5-2022

Mechanochromic Tunable Emissions of Hydrogel Encapsulated Radioluminescent Crystalline Colloidal Arrays

Sarah Mell
smell@clemson.edu

Mechanochromic Tunable Emissions of Hydrogel Encapsulated Radioluminescent Crystalline Colloidal Arrays

---

A Thesis
Presented to
the Graduate School of
Clemson University

In Partial Fulfillment
of the Requirements for the Degree
Master of Science
Materials Science and Engineering

---

by
Sarah Elizabeth Mell
May 2022

Accepted by:
Dr. Stephen Foulger, Committee Chair
Dr. Igor Luzinov
Dr. Kimberly Weirich

Abstract

Crystalline colloidal arrays (CCAs) are periodic dielectric arrays composed of monodisperse, negatively charged nanoparticles with unique optical characteristics. Poly(styrene-co-propargyl acrylate) (PS-PA) based copolymer nanoparticles synthesized via an emulsion polymerization form the basis of the CCAs in this work. The negatively charged surfaces result in the colloidal nanoparticles self-assembling into a face-centered cubic (fcc) crystal-like structure. The long-range order and spatial periodicity of the array result in a rejection wavelength, characteristic of CCAs, in which a specific wavelength of light is forbidden from propagating throughout the optical system. The CCAs exhibit mechanochromism through a rejection wavelength shift corresponding to a change in the interplanar spacing of the CCAs. The PS-PA particle basis in this work was modified by covalently incorporating organic emitters during synthesis to produce scintillating CCAs. CCA particles were copolymerized with a radioluminescent dye and additional fluorescent dyes to produce emissions across the visible light spectrum, forming three unique sets of CCA particles. Due to the liquid CCA system being sensitive to mechanical stress and ionic impurities, a poly(ethylene glycol) methacrylate (PEGMA) based hydrogel network was photopolymerized in situ with the CCAs to form a more mechanically robust film. By coupling the rejection wavelength with the radioluminescence, the encapsulated CCAs were demonstrated to have tunable emissions. The particular optical characteristics

of the fully organic, hydrogel encapsulated, radioluminescent CCAs result in possible future use as potentially less toxic x-ray bioimaging materials.

Dedication

To Kaitlin and Nikole for being the best support system I ever could have asked for. I thank both of you for always reminding me to stop and laugh a bit along the way and for believing in my success enough to convince me to maybe do the same. I must also thank my family for building me into the woman I am today; I would not have made it this far without you.

Acknowledgments

First and foremost, I want to thank Clemson University for giving me the opportunity to further my education with graduate studies, as well as the Materials Science and Engineering department for having me as a student for six years now. Special acknowledgement must also be given to Laura Kinard for pushing me to consider graduate school in the first place and always being willing to lend a hand when I needed it.

To Dr. Foulger, Dr. Luzinov, and Dr. Weirich: thank you all so much for serving on my committee and providing advice along the way. Working through a pandemic has been trying at times, so the patience and flexibility you all have shown me are greatly appreciated.

I would like to acknowledge my advisor, Dr. Stephen Foulger, for accepting me into his group and introducing me to the project on which the research presented in this thesis is focused. I thank all the members of my lab group for being so much more than just a lab group; you all brightened my days in a million different ways, from answering my lab questions all the way to hosting gameday brunches. Ben, Haley, Travis, Eric, and Yura: working with you all for the past year and a half has been a joy.

My work would not have been possible without the resources and funding provided by the National Science Foundation, Gregg-Graniteville Foundation, Cen-

ter for Optical Materials Science and Engineering Technology (COMSET), and the Materials Science and Engineering department.

Finally, I have so many people in my personal life that have uplifted me throughout this process and everything that came before it to get me here. To my parents: *you guys sure know how to raise some successful kids.* To my sister, Mary: *you've been a close friend when I needed it and a healthy rival at other times.* To my best friend, Nikole: *thanks for being my semi-random roommate, Clemson would never have been the same without you.* To my Kaitie: *every day I am thankful for your friendship; you're my rock.* To all of you and those I didn't mention, once again: *thank you.*

Table of Contents

Title Page . . . . . **i**

Abstract . . . . . **ii**

Dedication . . . . . **iv**

Acknowledgments . . . . . **v**

List of Tables . . . . . **ix**

List of Figures . . . . . **x**

1 Introductory Material **1**
1.1 Motivation 1
1.2 Background information 1
1.2.1 Mechanism of scintillation for organic compounds 1
1.2.2 Förster resonance energy transfer (FRET) pairing of organic emitters 3
1.3 Crystalline colloidal arrays (CCAs) 6
1.3.1 Hydrogel encapsulated crystalline colloidal arrays 7
1.3.2 Applications of CCAs 8

2 Materials, Syntheses, and Methods **10**
2.1 Chemical supplies 10
2.2 Syntheses of CCA series 10
2.2.1 S_1 CCA copolymer nanoparticles 10
2.2.2 S_2 CCA copolymer nanoparticles 12
2.2.3 S_3 CCA copolymer nanoparticles 13
2.3 Preparation of glass cells 13
2.4 Encapsulation in hydrogel network 13
2.5 Optical characterization methods 14

3 Mechanochromic Response of Encapsulated Crystalline Colloidal Arrays for Tunable Emissions **15**

3.1 Attributions . . . 15
3.2 Optical Properties of Crystalline Colloidal Arrays Encapsulated in Hydrogel Networks . . . 15
3.2.1 X-ray radioluminescence of CCA films . . . 16
3.2.2 The partial photonic bandgap . . . 20
3.3 Coupling the rejection wavelength with the radioluminescence of the system . . . 23
3.3.1 Radioluminescence spectra . . . 25
3.3.2 Difference in emissions . . . 26

4 Final Remarks . . . 29
4.1 Conclusion . . . 29
4.2 Future Work . . . 30

Appendices . . . 32
A Synthesis of organic emitter compounds . . . 33
A.1 Anthracene methyl methacrylate derivative (AMMA) . . . 33
A.2 Naphthalimide methyl methacrylate derivative (NMMA) . . . 34
A.3 Rhodamine B methyl methacrylate derivative (RMMA) . . . 35

Bibliography . . . 37

List of Tables

3.1 Change in lattice parameters for hydrogel encapsulated CCA as rejection wavelength is blue shifted. 21

List of Figures

1.1 Scintillation mechanism for an organic material such as anthracene. 2
1.2 Example of required spectral overlap for FRET transfer in which emission of the donor partially covers the same region as the absorption of the acceptor. 4
1.3 Absorption (blue) and photoluminescence (pink) spectra for organic emitters in aniline: a) anthracene (crystalline anthracene for photoluminescence), b) azide modified naphthalimide, and c) rhodamine B. Figure adapted from reference [1] with permission. 5
1.4 Representation of CCA with fcc structure. 6
1.5 Schematic for encapsulation of CCA particles in hydrogel network via in situ polymerization. Hydrogel stabilizes self-assembled colloidal particles. 8

2.1 Reaction mechanism for synthesis of PS-PA based radioluminescent nanoparticles with AMMA covalently incorporated. 12

3.1 Typical radioluminescence characteristic of S_1 CCA films (AMMA incorporated). Radioluminescence spectra collected from hydrogel encapsulated CCA with rejection wavelength beyond the range of emission. 16
3.2 Typical radioluminescence characteristic of S_2 CCA films (AMMA, NMMA incorporated). Radioluminescence spectra collected from hydrogel encapsulated CCA with rejection wavelength beyond the range of emission. 18
3.3 Typical radioluminescence characteristic of S_3 CCA films (AMMA, NMMA, RMMA incorporated). Radioluminescence spectra collected from hydrogel encapsulated CCA with rejection wavelength beyond the range of emission. 19
3.4 Shift in rejection wavelength of hydrogel encapsulated CCA film observed as reflectance. The rejection wavelength was blue-shifted by drying the film. 20
3.5 Rejection wavelength of hydrogel encapsulated CCA reversibly shifted from ca. 550 nm to ca. 425 nm and back to ca. 540 nm by method of drying and rehydrating hydrogel network. 22
3.6 Radioluminescence sprectra for all three sets of CCA particles encapsulated in a hydrogel network comparing emission before and after the rejection wavelength is shifted to overlap the targeted emitter. (a) S_1 CCA film with rejection wavelength at 428 nm and 525 nm, (b) S_2 film with rejection wavelength at 517 nm and 551 nm, and (c) S_3 film with rejection wavelength at 617 nm and 746 nm. 24

3.7 Difference between the emission spectra for films of each CCA series compared to the rejection wavelength corresponding to the suppressed emission; reflectance observed from a small area of the CCA film. (a) S_1 CCA film with reflectance (blue) at 428 nm, (b) S_2 film with reflectance (green) at 517 nm, and (c) S_3 film with reflectance (red) at 617 nm. 27
3.8 The percentage of initial emission blocked at each point based on the two spectra from **Figure 3.6**. (a) S_1 CCA film, (b) S_2 film, and (c) S_3 film. 28

1 Synthetic scheme to yield anthracen-9-ylmethyl methacrylate (AMMA). 33
2 Synthetic scheme to yield 1,3-dioxo-6-(piperidin-1-yl)-1H-benzo[de]isoquinolin-2(3H)-yl)ethyl methacrylate (NMMA). 34
3 Synthetic scheme to yield N-(6-(diethylamino)-9-(2-((2-(methacryloyloxy)ethoxy)carbonyl)phenyl)-3H-xanthen-3-ylidene)-N-ethylethanaminium chloride (RMMA). 36

Chapter 1

Introductory Material

1.1 Motivation

X-ray bioimaging frequently requires toxic, heavy metal contrast agents to produce an image, so there is an interest in developing a fully organic, potentially less harmful imaging probe utilizing scintillators [1, 2, 3, 4, 5, 6, 7]. Colloidal nanoparticles are favorable for biological applications due to their high stability in aqueous solution and ability for modification [8, 9]. Pairing fully organic colloidal nanoparticles with organic scintillators may lead to less-toxic x-ray imaging probes, as opposed to previously designed nanoparticle probes functionalized with toxic imaging agents [10, 11, 12].

1.2 Background information

1.2.1 Mechanism of scintillation for organic compounds

The radioluminescent materials in this work depend on the scintillating mechanism of an organic compound. Inorganic scintillators can be much brighter but

require a regular crystalline lattice to fluoresce, while organic scintillators can be used in a variety of states such as vapor, polycrystalline solid, liquid solution, solid solution, or part of a composite [13, 14, 15]. Instead of relying on bulk properties of the material, the scintillating mechanism of an organic scintillator is based on the electronic structure and vibrational states of the molecule itself, often associated with symmetry and aromaticity [14]. The resonance within a benzene ring results in six completely delocalized π orbitals; it is the excitation of the π-electron systems in similar polycyclic aromatic molecules that leads to the luminescence exhibited by these compounds [13, 14]. The π-electron energy levels and photochemical processes for an organic polycyclic molecule are shown in **Figure 1.1**.

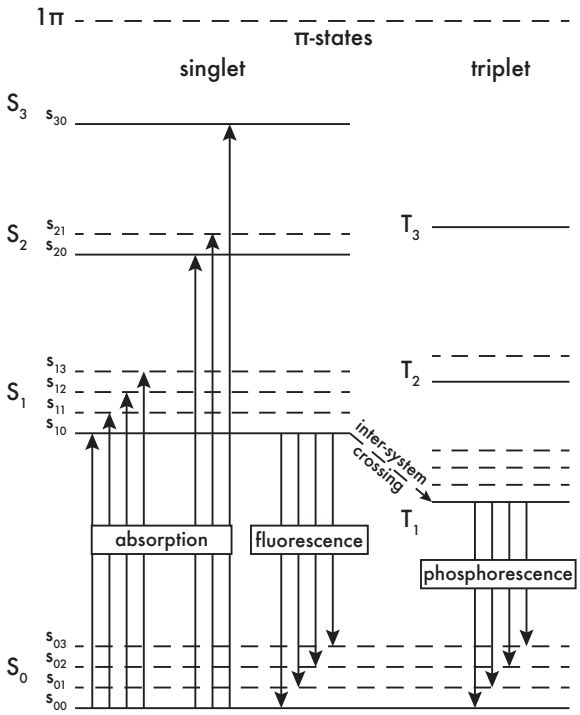

Figure 1.1: Scintillation mechanism for an organic material such as anthracene.

For a scintillating material, electrons are promoted to elevated energy states when energy is absorbed from ionizing radiation, such as x-rays [16]. The energy of an excited electron is dissipated primarily in a nonradiative fashion, such as through heat loss or lattice vibrations, while a small portion is released radiatively through conversion into fluorescent energy [13]. Regarding the radiative transfer, as the electrons return to lower level energy states, the released energy is observed as short flashes of light with wavelengths in or near the visible spectrum [14, 16]. Effectively, scintillators convert high-energy ionizing radiation into visible light. Anthracene has one of the highest scintillating efficiencies of all organic scintillators, with a characteristic three-pronged emission featuring a shoulder in the blue light region upon irradiation with x-rays [13, 17, 18]. The multi-pronged emission peak is caused by the several vibrational bands exhibited by an aromatic organic scintillator with an energy level structure similar to that shown in **Figure 1.1** [13, 19]. Because of its relative brightness, anthracene was chosen as the organic scintillator to be used in this work.

1.2.2 Förster resonance energy transfer (FRET) pairing of organic emitters

The mechanism for the transfer of excitation energy between donor and acceptor pairs is dependent on the spacing between the molecules [20]. The transfer is nonradiative when the particles are sufficiently near each other, typically of the order of 5 nm apart; otherwise, the transfer is radiative [21]. Both transfer methods are facilitated by interaction between the dipole moments of the molecules, but the nonradiative transfer involves near-field components of the dipole while the radiative transfer happens via the far-field [20, 22]. The radiationless transfer is known

as Förster resonance energy transfer (FRET), and compounds exhibiting this transfer are known as FRET pairs. In order for FRET to occur, there must be spectral overlap between the emission of the donor and the absorbance of the acceptor (cf. **Figure 1.1**). An increased efficiency in energy transfer is observed with a greater area of spectral overlap [23].

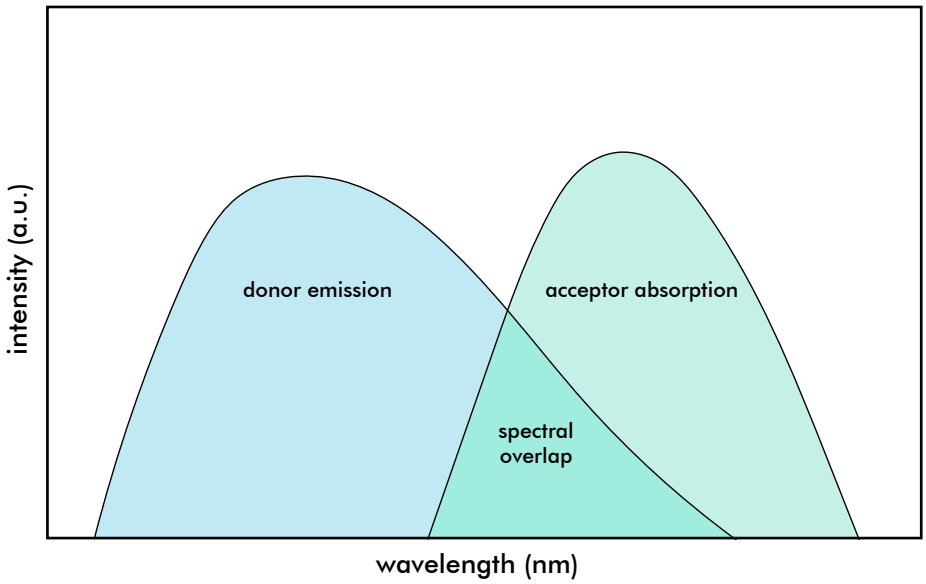

Figure 1.2: Example of required spectral overlap for FRET transfer in which emission of the donor partially covers the same region as the absorption of the acceptor.

FRET pairing of emitters can tailor the emission properties of a radioluminescent system to span the entire visible light spectrum. Fluorescent dyes, or materials that both absorb and emit in the visible light spectrum, can be coupled with scintillators demonstrating spectral overlap to alter the region in which photons are radiatively emitted. In this work, sequential FRET pairing was used to develop radioluminescent systems that emitted in the blue, green, and red light regions by covalently incorporating organic emitters into copolymer nanoparticles. The first FRET pair coupled an anthracene derivative (organic scintillator) with a naphthalimide deriva-

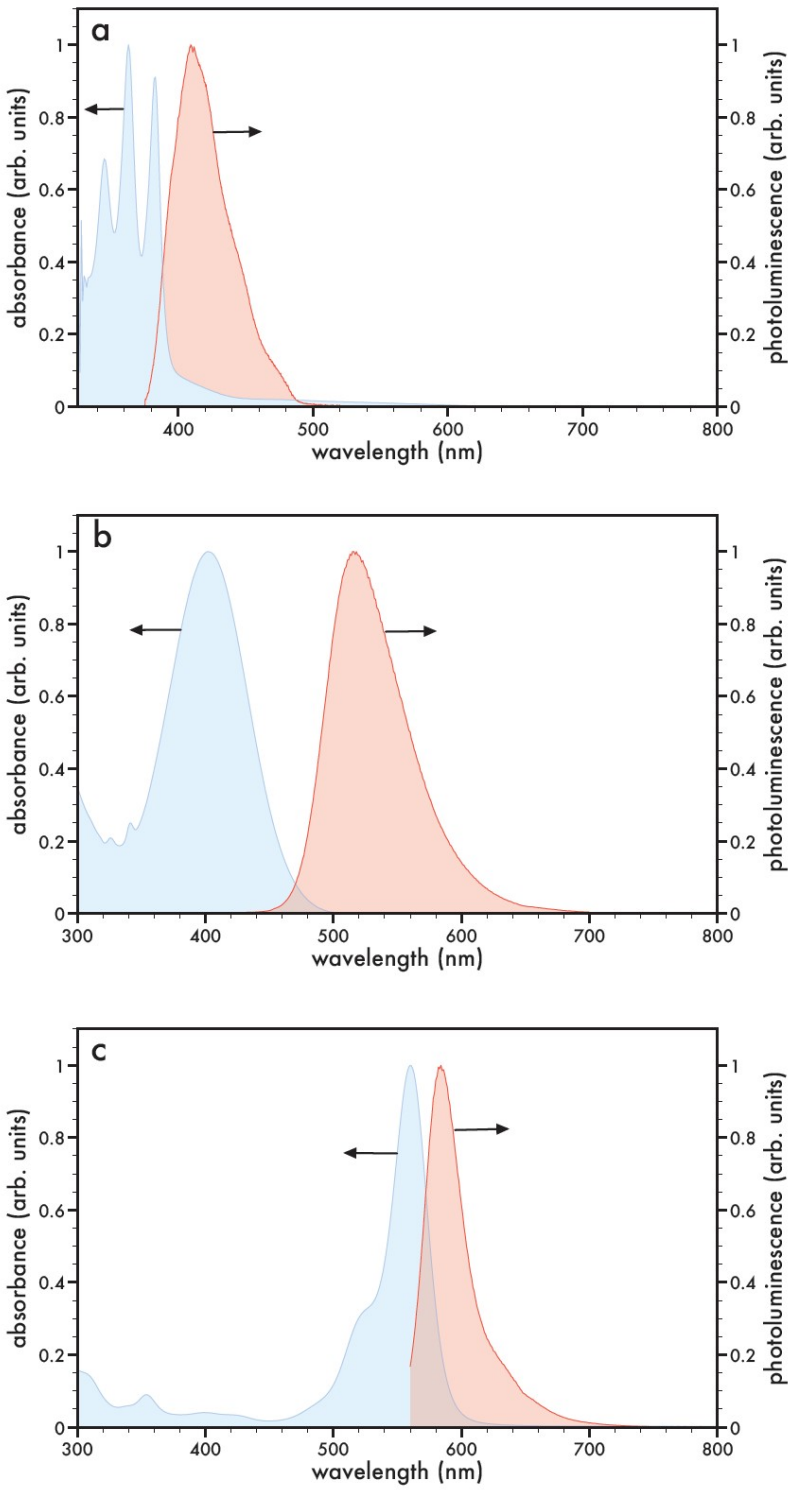

Figure 1.3: Absorption (blue) and photoluminescence (pink) spectra for organic emitters in aniline: a) anthracene (crystalline anthracene for photoluminescence), b) azide modified naphthalimide, and c) rhodamine B. Figure adapted from reference [1] with permission.

tive (organic fluorescent dye) that absorbs in the blue light region and emits in the green region. Due to the significant spectral overlap exhibited by these compounds, upon x-ray irradiation, the donor (anthracene) was excited, and the energy was subsequently transferred to the acceptor (naphthalimide) for an overall green emission of the system. Another organic fluorescent dye, a rhodamine B derivative, was similarly incorporated for its absorption in the green light region and emission in the red light region. Incorporating all three organic emitters leads to a sequential energy transfer upon irradiation of the system from the excited anthracene to each fluorescent dye in turn. The absorption and photoluminescence spectra for similar organic compounds to those used in this work are shown in **Figure 1.1**, which clearly demonstrates the spectral overlap for each of the pairings.

1.3 Crystalline colloidal arrays (CCAs)

Crystalline colloidal arrays (CCAs) have long been of interest for their unique optical characteristics [24, 25, 26, 27, 28]. These periodic dielectric arrays are composed of electrostatically stabilized colloidal nanoparticles that are frequently polystyrene or silica based [29]. Negatively charged surfaces of the particles result in long-range electrostatic repulsion forces that induce spontaneous self-assembly into a crystal-like structure in aqueous media [30]. The array can be either face-centered cubic (fcc) or body-centered cubic (bcc), depending on the minimum energy configuration [31, 32]. This thermodynamically favored state is in-

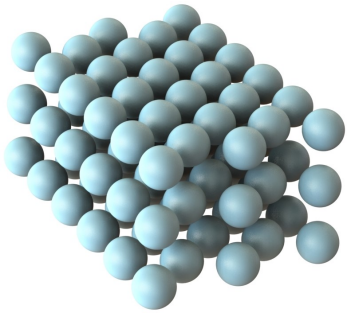

Figure 1.4: Representation of CCA with fcc structure.

herently dependent on the concentration or packing density of the particles comprising the colloid [33]. The CCAs presented in this effort are sufficiently concentrated so as to assemble into an fcc structure. The long-range ordering and spatial periodicity cause CCAs to exhibit optical iridescence similar to that of the naturally occurring precious opal gemstone [34]. The periodicity also results in a partial photonic bandgap in which specific wavelengths of light are forbidden from propagating throughout the material [28]. The rejection wavelength is inherently dependent on the angle of incidence and is sensitive to the interplanar spacing of crystalline structure [26, 35]. Interparticle spacing of the order of 100 nm results in the exhibited bandgap residing in the visible light or near-infrared regime [36, 37].

1.3.1 Hydrogel encapsulated crystalline colloidal arrays

The crystalline ordering of the liquid CCAs is fragile; there can be a temporary destruction of the array from applied mechanical stress after which self-assembly may occur once again, or permanent disorder from ionic impurities being introduced [28]. To resolve these issues and convert the liquid CCAs into a more mechanically robust film, the system can be encapsulated in a hydrogel network to stabilize the crystal structure with insignificant effects on the unique optical properties [27, 28, 29, 38]. Converting the fluid optical system into a hydrogel film is favorable for portability and relative ease of handling. The encapsulation in a polymer hydrogel network prevents the destruction of the crystal structure while enabling interplanar spacing to be manipulated by the volume of the hydrogel. Various bases for the hydrogel network have been used to entrap the CCA structure, commonly including crosslinked networks of poly(methyl methyacrylate) (PMMA) [25], acrylamides [27], or poly(ethylene glycol) methacrylate (PEGMA) [28, 39]. In this work, a crosslinked

PEGMA based hydrogel network was photopolymerized in situ with the CCA since poly(ethylene glycol) is well-known to be biologically compatible and is extremely common for biomedical applications [40].

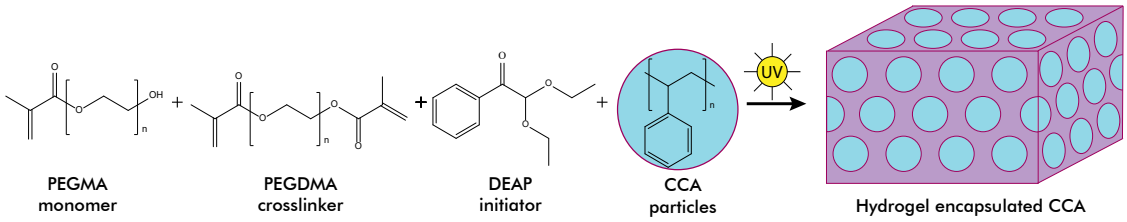

Figure 1.5: Schematic for encapsulation of CCA particles in hydrogel network via in situ polymerization. Hydrogel stabilizes self-assembled colloidal particles.

1.3.2 Applications of CCAs

Due to selective light transmission, CCAs have promising potential as detectors or optical rejection filters [41]. Since the partial photonic bandgap is dependent on the spacing of the array, volume changes of hydrogel encapsulated CCAs have been exploited to develop efficient sensors for a variety of biological applications such as monitoring glucose [42, 43], determining lead concentration [44, 45], and measuring creatinine levels [46]. To develop these sensors, the CCAs are modified with stimuli-responsive functional groups or materials that will shift the rejection wavelength as a function of the subject of interest. For example, a glucose recognition material was developed by incorporating phenylboronic acids into CCA hydrogels [42, 43]. Glucose molecules reversibly bind to the phenylboronic acids, which leads to an increase in the crosslink density of the hydrogel. Increased crosslinking results in the film shrinking, decreasing the interplanar spacing of CCAs and producing a blue-shift in the diffracted wavelength corresponding with higher glucose concentration. A

crown ether chelating agent for Pb^{2+} ions incorporated into a CCA hydrogel produces a similar effect to that in the glucose-sensing device. The chelating agent resulted in a Donnan potential being produced and resulted in a swelling of the gel and a longer rejection wavelength corresponding to the concentration of lead ions [44]. Minor adjustments were made to both the glucose- and lead-sensing devices to allow them to function accurately in environments of varying ionic strength, such as in both tear fluid and blood [43, 45]. Various mechanisms to alter the interplanar spacing have been developed, including those which change the hydrogel volume based on pH [47, 48], temperature [49], and mechanical stresses [28, 50].

Introducing a scintillator into the CCA system expands the potential functionality to encompass x-ray imaging methods such as x-ray fluorescence computed tomography (XFCT), which depends on the selective excitation of radioluminescent nanoparticles [51]. The incorporated scintillators can be paired with fluorescent dyes to control the wavelength at which the CCAs emit [39, 52]. The luminescent materials impart radioluminescent properties to the optical system as a whole. Prior work regarding scintillating encapsulated CCAs incorporates organic emitters after hydrogel encapsulation [39]; however, in the effort presented here, the emitters are covalently incorporated during the emulsion copolymerization of the CCA nanoparticles.

Chapter 2

Materials, Syntheses, and Methods

2.1 Chemical supplies

Deionized (DI) water was sourced from a Nanopure Diamond System with a resistivity reading of 18.2 MΩ·cm. Reagents and solvents were bought from commercial suppliers (e.g., Sigma-Aldrich). Monomers used in the synthesis of crystalline colloidal arrays (CCAs) were cleaned via filtering through aluminum oxide (Al_2O_3). Mixed-bed ion exchange resin (BioRad Laboratories, AG 501-X8 Resin, 20-50 mesh) beads were mixed with monomers used in the hydrogel network for at least one day before using.

2.2 Syntheses of CCA series

2.2.1 S_1 CCA copolymer nanoparticles

Poly(styrene-co-propargyl acrylate-co-anthracene methyl methacrylate) (PS-PA-PAMMA) CCA nanoparticles (S_1) described in this paper were synthesized via emulsion copolymerization. The emitter was added such that 0.5 w/w% of the an-

thracene compound (0.067 mg AMMA) was dissolved in purified styrene monomer (14.72 mL, or 13.336 g) by sonicating the mixture. 50 mL of DI water, 25% of the styrene-AMMA mixture (3.68 mL), and 25% of the propargyl acrylate (0.32 mL) were then added to a 4-neck round bottom flask. The remaining 75% of the previous components were added to a dropping funnel and affixed to one of the necks of the round bottom flask while a mechanical stirrer and thermocouple were attached to another neck. Stirring was set to 370 rpm, and the contents of the round bottom flask were purged with nitrogen below the solution level for 40 minutes. The purge gas was then moved above the solution line, and the temperature was increased to 60°C. Sodium lauryl sulfate (0.18 mL, 29% by mass in DI water) and divinylbenzene (0.1 mL) were injected into the flask, and the temperature was allowed to stabilize. Once the reaction vessel reached temperature, solutions of sodium hydrogen phosphate (Na_2HPO_4, 0.14 g in 0.8 mL of DI water) and potassium persulfate ($K_2S_2O_8$, 0.14 g in 1.0 mL of DI water) were injected into the round bottom flask. The temperature was then increased to 71°C and allowed to stabilize for 20 minutes. The contents of the dropping funnel were then allowed to drip into the reaction vessel at a rate of 1 drop every 2 seconds. When half of the contents of the dropping funnel had been added, more divinylbenzene (0.24 mL) was injected into the reaction. Once the dropping funnel was emptied, the reaction was allowed to proceed for 2.5 hours. The reaction was cooled to 37°C, and the product was cleaned by gravity filtering. The filtered product was then transferred into dialysis bags (50,000 MWCO) and dialyzed in a DI water bath, changed frequently until opalescence was observed, roughly two weeks. The opalescence indicates the self-assembly of the particles into a CCA. After shaking for two days with ion exchange resin beads in a Nalgene bottle, the CCA was stored at room temperature. The diameter of the particles was measured to be 123.4 $\pm$ 13.4 nm through dynamic light scattering (DLS, Coulter N4Plus dynamic

light scatter). The zeta potential of the CCA was -66.99 mV and was measured with a ZetaPlus zeta potential analyzer (Brookhaven Instruments Corp.).

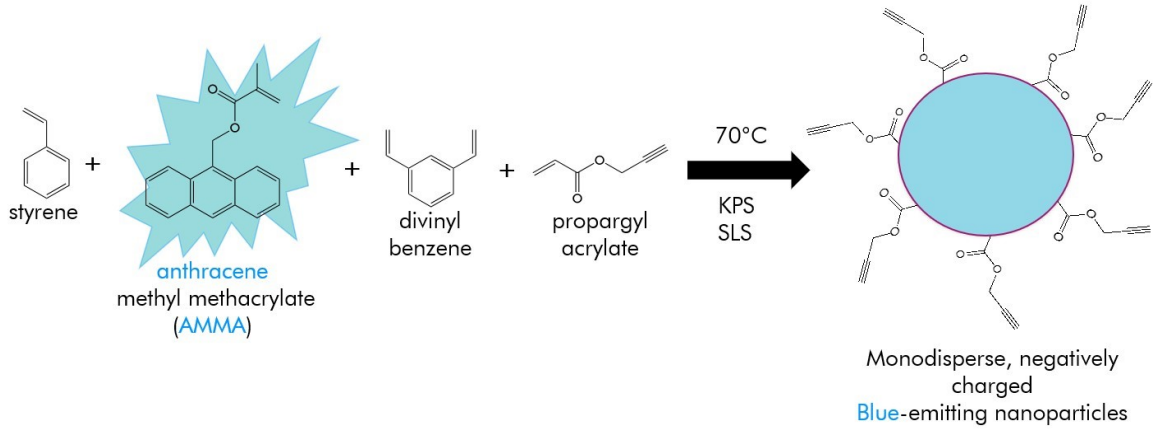

Figure 2.1: Reaction mechanism for synthesis of PS-PA based radioluminescent nanoparticles with AMMA covalently incorporated.

2.2.2 S_2 CCA copolymer nanoparticles

A similar procedure to that of the previous section was performed to synthesize the poly(styrene-co-propargyl acrylate-co-anthracene methyl methacrylate-co-naphthalimide methyl methacrylate) (PS-PA-PAMMA-PNMMA) with AMMA and NMMA (CCA S_2). At the point in the procedure in which the emitter compound is dissolved in the styrene monomer, 0.3 w/w% AMMA and 0.3 w/w% naphthalimide methyl methacrylate derivative (NMMA) were dissolved into the styrene monomer by dissolving each emitter into half of the total styrene monomer (40 mg of emitter into 7.36 mL of styrene). The remaining procedure was performed the same as previously described. The size of the particles was 123.6 $\pm$ 23.0 nm with a zeta potential of -50.50 mV.

2.2.3 S_3 CCA copolymer nanoparticles

To synthesize the poly(styrene-co-propargyl acrylate-co-anthracene methyl methacrylate-co-naphthalimide methyl methacrylate-co-rhodamine B methyl methacrylate) (PS-PA-PAMMA-PNMMA-PRMMA) particles with all three emitters (CCA S_3), the same procedure as the previous section was performed with the addition of a rhodamine B compound, such that 0.3 w/w% AMMA, 0.3 w/w% NMMA, and 0.3 w/w% of a rhodamine B methyl methacrylate derivative were dissolved each into a third of the total styrene monomer. The rest of the procedure was kept the same. For each emitter, 40 mg were dissolved in 4.906 mL of styrene. The size of the particles was 155.1 $\pm$ 14.5 nm with a zeta potential of -70.77 mV.

2.3 Preparation of glass cells

The glass cells were prepared according to a previously described method [39]. In brief, the surface of Corning glass slides was modified to be hydrophobic via a treatment using an octadecyltrichlorosilane (OTS) and toluene solution. Two slides were separated with a spacer cut from 2 adhered pieces of Parafilm to form a 2 cm $\times$ 1 cm $\times$ 250 μm cavity.

2.4 Encapsulation in hydrogel network

The CCAs were encapsulated in a poly(ethylene glycol) methacrylate (PEGMA) based hydrogel network via in situ photopolymerization. The hydrogel matrix materials included the PEGMA monomer, poly(ethylene glycol) dimethacrylate (PEGDMA) cross-linker, and 2,2-diethoxyacetophenone (DEAP) photoinitiator in 10:1:0.1 ratio, respectively. Typically, 300 μL of CCA in DI water was combined with 55 μL of

PEGMA, 5.5 μL of PEGDMA, and 0.6 μL of DEAP. The matrix materials were mixed with the CCA in a cuvette and shaken until opalescence was observed for the whole mixture, usually overnight. Approximately 60 μL of the CCA-hydrogel mixture were then injected into a glass cell. The cell was then exposed to a UV source (ELC-500 Light Exposure System, Electro-Lite Corporation) for 4 minutes to photopolymerize the matrix surrounding the CCA. Finally, the hydrogel encapsulating the CCA was removed from the glass cell and stored in DI water.

2.5 Optical characterization methods

Reflectance spectra were collected using a Perkin Elmer Lambda 950 spectrophotometer. To irradiate the CCAs encapsulated in hydrogel films, an Amptek Mini-X X-ray unit equipped with a tungsten target was used while operating at 25 kV and 158 μA. Radioluminescence spectra of the hydrogel films were collected via a cooled CCD detector (Synapse, Horiba Jobin-Yvon) and a MicroHR monochromator (Horiba Jobin-Yvon). The radioluminescence spectra were collected from a slit width of 1 mm over an exposure time between 45 seconds to 90 seconds and the signal collected with a blaze of 500 nm and with a 600 line mm^{-1} grating. The radioluminescence spectra was collected on the (111) plane of the CCA without accounting for the emission of the donor. Horiba Jobin-Yvon SynerJY was the software used to analyze the data collected. The CCA films were dried on top of poly(methyl methacrylate) (PMMA) for data collection because it is optically clear and does not have a signature within the visible light spectrum when irradiated, allowing for observation of the film without interference.

Chapter 3

Mechanochromic Response of Encapsulated Crystalline Colloidal Arrays for Tunable Emissions

3.1 Attributions

The synthesis and characterization of the organic emitters used in this work (AMMA, NMMA, and RMMA) were performed by Dr. Yura Bandera. CCA series S_2 and S_3 were synthesized by Haley Jones.

3.2 Optical Properties of Crystalline Colloidal Arrays Encapsulated in Hydrogel Networks

An organic scintillator and fluorescent dyes were covalently incorporated into monodisperse copolymer nanoparticles via emulsion copolymerization to form x-ray

radioluminescent nanoparticles. The emitters were used in combination to manipulate the nanoparticles into emitting in various regimes across the visible light spectrum when excited via x-rays as shown in **Figures 3.1 – 3.3**. The particles also exhibited a rejection wavelength, characteristic of CCA particles, which was manipulated to shift across the visible light spectrum.

3.2.1 X-ray radioluminescence of CCA films

Three unique series of radioluminescent CCA particles were synthesized in this work, differentiated by the combination of organic emitters incorporated. The particle sets employed a base radioluminescent dye that acted as the "pump source" for additionally incorporated fluorescent dyes, which formed Förster resonance energy

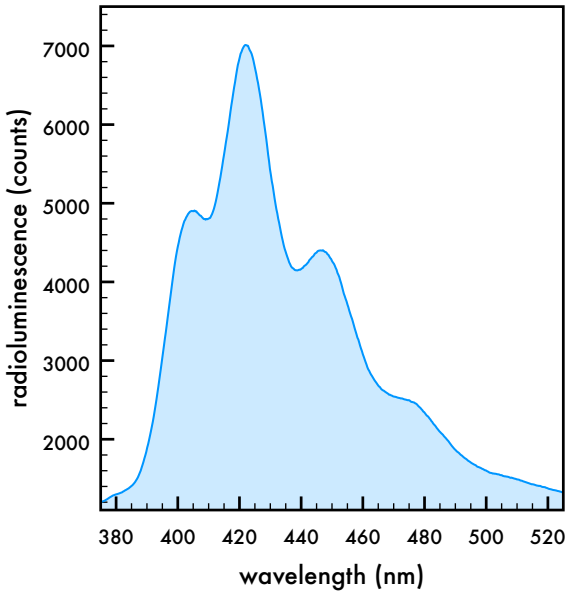

Figure 3.1: Typical radioluminescence characteristic of S_1 CCA films (AMMA incorporated). Radioluminescence spectra collected from hydrogel encapsulated CCA with rejection wavelength beyond the range of emission.

transfer (FRET) pairs. The first set of CCA particles (S_1) covalently incorporated only the base radioluminescent dye, which was a derivative of anthracene, a well-known organic scintillator, specifically anthracene methyl methacrylate (AMMA). Anthracene was selected because it is the brightest organic scintillator and emits in the blue region of the visible light spectrum upon irradiation [13, 53]. Following encapsulation in a hydrogel network, the S_1 CCA excited with x-rays displayed a radioluminescence spectrum spanning ca. 390 nm to 500 nm, with peaks at 409 nm, 424 nm, 449 nm and a shoulder at 480 nm, and is presented in **Figure 3.1**. The three-pronged peak with accompanying shoulder is characteristic of anthracene, indicating that the CCA system exhibits the emission characteristic of the incorporated scintillator [14, 13, 19, 53].

$$E = 1 - \frac{I_D}{I_D + I_A} \tag{3.1}$$

The second set of particles (S_2) incorporated AMMA and a fluorescent dye, naphthalimide methyl methacrylate (NMMA), which emits green light when excited. As discussed previously, naphthalimide forms a Förster resonance energy transfer (FRET) pair with anthracene. The FRET pairing leads to an energy transfer between the emitters when both are incorporated into a CCA particle set, in which the AMMA acts as the donor and the NMMA as the acceptor. The resulting radioluminescence after irradiating the hydrogel encapsulated S_2 CCA is shown in **Figure 3.2**; the emission spanning from ca. 450 nm to 600 nm with a strong, rounded peak at 511 nm is characteristic of an excited naphthalimide compound [54]. There is no signature of anthracene emission in the collected radioluminescence spectra, suggesting an efficient energy transfer between the AMMA and NMMA. The calculated energy transfer efficiency for AMMA to NMMA is 97.0% according to the standard equation for

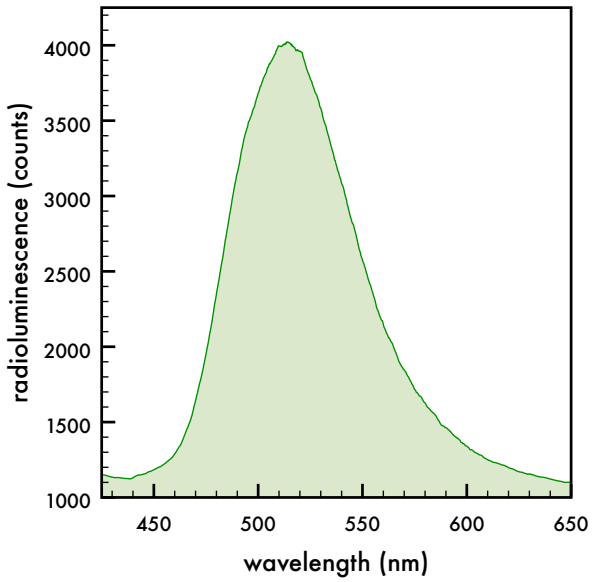

Figure 3.2: Typical radioluminescence characteristic of S_2 CCA films (AMMA, NMMA incorporated). Radioluminescence spectra collected from hydrogel encapsulated CCA with rejection wavelength beyond the range of emission.

FRET efficiency, Equation 3.1, where I_D and I_A are the intensities of the donor and the acceptor [55]. The intensities values were obtained from the integral of the emission curve for the range of each incorporated emitter. For this pairing, the range for AMMA emission was chosen to be $\lambda < 450$ nm, and for NMMA 450 nm $\leq \lambda < 600$ nm.

The last CCA series (S_3) covalently incorporated AMMA, NMMA, and another fluorescent dye, a rhodamine B methyl methacrylate (RMMA) derivative. Similar to the previous emitter coupling, rhodamine B is a FRET pair with naphthalimide, such that the excited NMMA (donor) transfers energy to RMMA (acceptor). When all three emitters are incorporated into a CCA system, there is a primarily red light emission with excitation of the system. The radioluminescence of the S_3 hydrogels when irradiated with x-rays was characterized by a short hump with a local maxi-

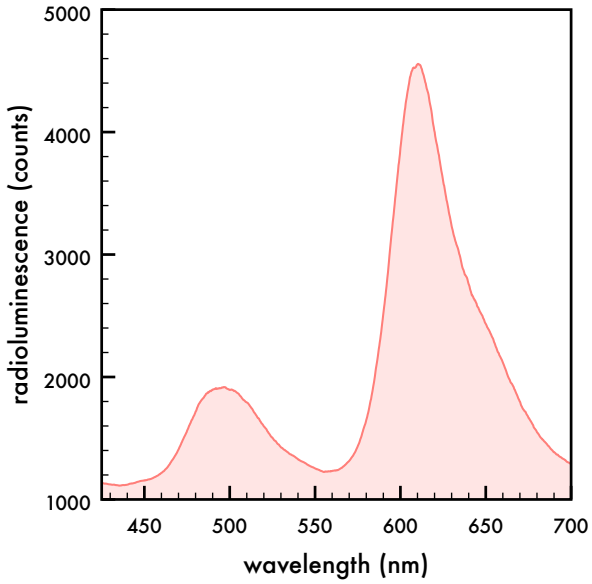

Figure 3.3: Typical radioluminescence characteristic of S_3 CCA films (AMMA, NMMA, RMMA incorporated). Radioluminescence spectra collected from hydrogel encapsulated CCA with rejection wavelength beyond the range of emission.

mum at 498 nm and a tall, narrow peak with a maximum at 611 nm, presented in **Figure 3.3**. The short hump is attributed to the emission of NMMA, while the tall peak is characteristic of rhodamine B emission [56]. This suggests that the energy transfer from the NMMA to the RMMA was not as efficient as the transfer between the first FRET pair. For the S_3 films, the energy transfer efficiency from AMMA to NMMA was found to be 96.7% and from NMMA to RMMA was 76.8%. In this case, the ranges of emission for each emitter used in calculating the energy transfer were $\lambda < 450$ nm for AMMA, 450 nm$\leq \lambda <$ 550nm for NMMA, and 550nm $\leq \lambda <$ 690 nm for RMMA.

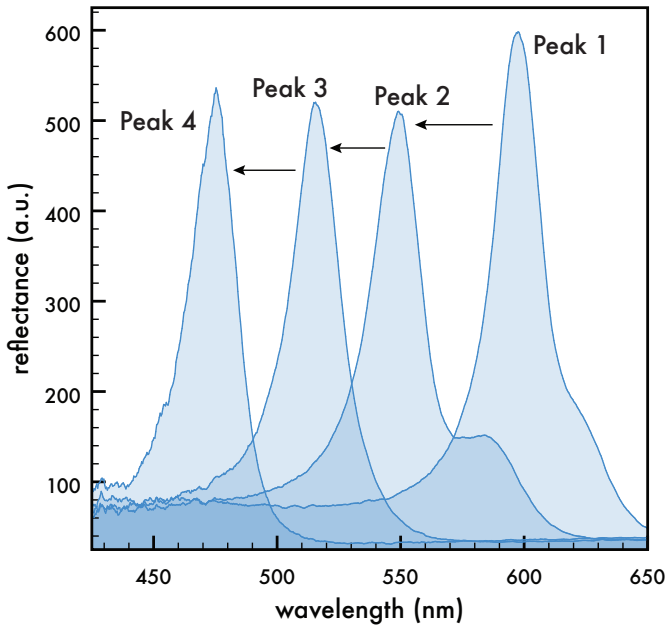

Figure 3.4: Shift in rejection wavelength of hydrogel encapsulated CCA film observed as reflectance. The rejection wavelength was blue-shifted by drying the film.

3.2.2 The partial photonic bandgap

The CCAs exhibit a rejection wavelength at which specific wavelengths of the visible light or near-infrared (NIR) spectrum are forbidden from propagating throughout the material due to the long-range ordering of the particles [28, 27, 25]. The rejection wavelength was observed via the reflectance of the material since only photons corresponding to the forbidden wavelength are not transmitted. The rejection wavelength can be estimated by using Bragg's Law:

$$\lambda_{rw} = 2n_c d_{hkl} \sin(\theta) \tag{3.2}$$

where λ_{rw} is the rejection wavelength, n_c is the refractive index characteristic of the composite, d_{hkl} is the interplanar spacing of the scattering planes, and θ is the angle

of incident light [26, 27]. Qualitatively, Braggs Law indicates that the rejection wavelength of the CCA particles is directly related to the interplanar spacing of the CCA, assuming that the refractive index and angle of incident light remain constant. The crystalline arrays exhibit mechanochromism, in which a mechanical alteration in the interparticle spacing, and thereby interplanar spacing, shifts the rejection wavelength along the visible light and NIR spectrum. For example, diluting the particles in the liquid CCA system with DI water demonstrates the mechanochromic properties of the arrays. The dilution decreases the concentration of the particles, resulting in a uniform increase in interparticle spacing and a longer rejection wavelength. Likewise, following encapsulation in a hydrogel network, the interparticle spacing of the CCA can be manipulated by controlling the volume of the hydrogel based on the water content.

Table 3.1: Change in lattice parameters for hydrogel encapsulated CCA as rejection wavelength is blue shifted.

	Peak 1	Peak 2	Peak 3	Peak 4
n_c	1.368	1.368	1.368	1.368
λ (nm)	598	549	515	475
d_{111} (nm)	218.6	200.7	188.2	173.6
a_c (nm)	378.6	347.5	326.0	300.7
a (nm)	267.7	245.8	230.5	212.6

As the hydrogel network shrinks while it is dried out, the CCA particles are brought closer together, resulting in a shorter rejection wavelength. **Figure 3.4** demonstrates a blue shift in the rejection wavelength from 598 nm to 475 nm by drying a CCA film on a PMMA substrate in air with 40% relative humidity, with reflectance spectra collected periodically throughout the shift. Bragg's Law was used to quantitatively assess parameters of the crystalline array by using a literature value for

the refractive index ($n_c = 1.368$), maintaining the angle of incidence ($\theta = 90°$), and the observed rejection wavelength[28]. Changes in the refractive index of the system were neglected. These values provide an approximation for the interplanar spacing of the (111) plane, which can be used to further evaluate the crystalline structure. The lattice parameter of a conventional cubic cell (a_c) is found with $a_c = \sqrt{3}d_{111}$ and the nearest neighbor spacing (a) is calculated as $a = a_c/\sqrt{2}$. **Table 3.1** contains the obtained values for d_{111}, a_c, and a for each reflectance peak in **Figure 3.4**. By shifting the rejection wavelength nearly 125 nm, the nearest neighbor distance was decreased by 20.6%. According to FRET theory, the distance required for an efficient energy transfer is generally in the range of $1 - 10$ nm [57]. The estimated inter-particle spacing within the CCAs found in **Table 3.1** eliminates the possibility for inter-particle FRET exchange, instead suggesting there is non-radiative energy transfer only on

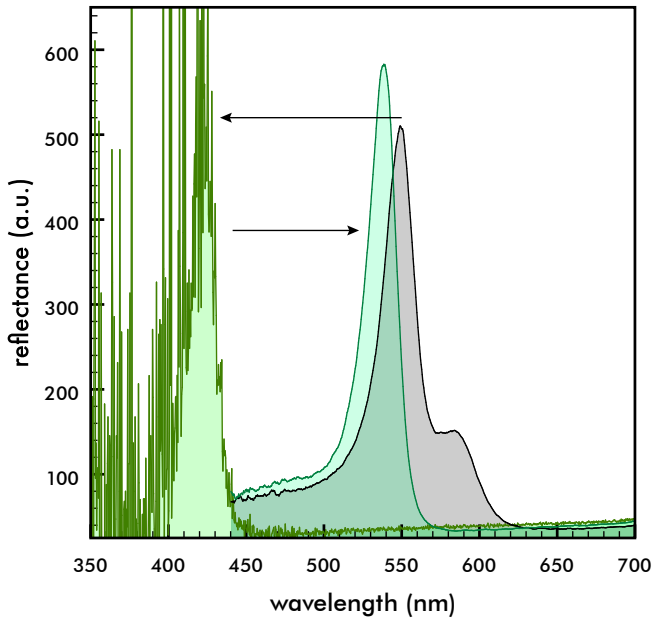

Figure 3.5: Rejection wavelength of hydrogel encapsulated CCA reversibly shifted from ca. 550 nm to ca. 425 nm and back to ca. 540 nm by method of drying and rehydrating hydrogel network.

the intra-particle scope. Similarly, because collected radioluminescence spectra did not significantly vary with volume changes of the system, it was concluded radiative inter-particle energy exchange was insignificant.

Additionally, shifting the rejection wavelength via altering the volume of the hydrogel network is a reversible process. After blue-shifting the partial bandgap by drying the film, DI water can be added across the surface in a uniform layer and allowed to absorb into the hydrogel network. The hydrogel networks swells as the DI water is absorbed, and the spacing between CCA particles expands. Following rehydration, the rejection wavelength is red-shifted back across the visible light spectrum towards its original position. This process is presented in **Figure 3.5**. The gray reflectance peak at ca. 550 nm is the initially observed rejection wavelength for a hydrogel-encapsulated CCA, which is then blue-shifted to the light green peak at ca. 425 nm and subsequently shifted back towards its initial emission after rehydration with a reflectance peak at ca. 540 nm, colored in darker green. After one cycle of drying and swelling, the rejection wavelength is nearly in the same position as to where it began, confirming the reversibility of the bandgap shift.

3.3 Coupling the rejection wavelength with the radioluminescence of the system

Due to the partial photonic bandgap forbidding all photons of a specific wavelength from propagating through the optical system, a decrease in the radioluminescence of the CCA series should be observed when the rejection wavelength is shifted to overlap the characteristic range of emission for a targeted emitter.

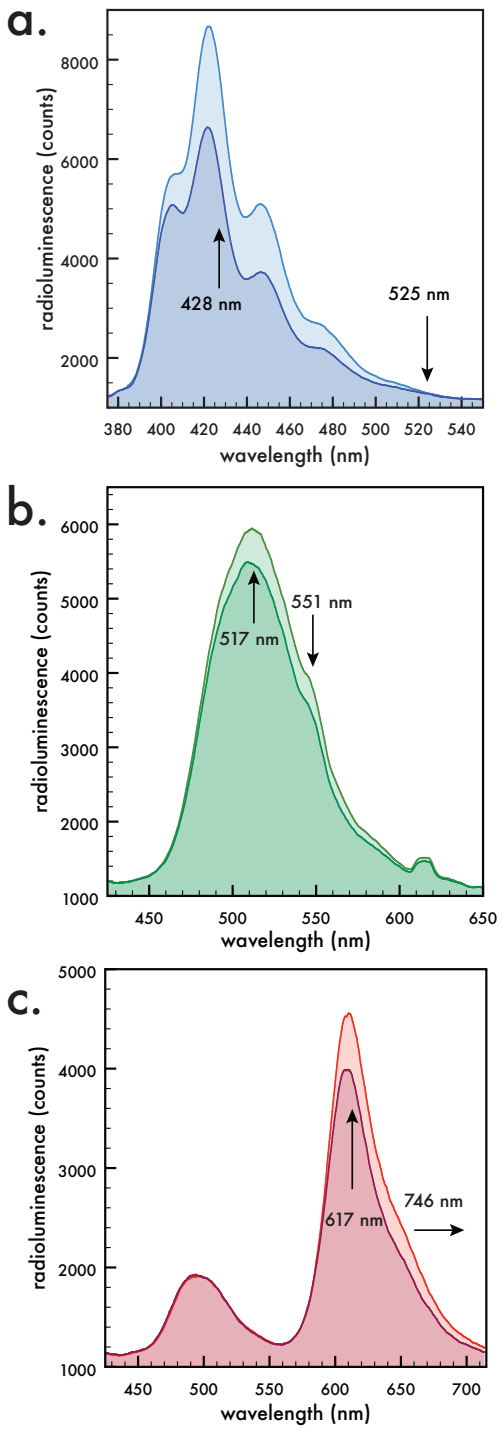

Figure 3.6: Radioluminescence sprectra for all three sets of CCA particles encapsulated in a hydrogel network comparing emission before and after the rejection wavelength is shifted to overlap the targeted emitter. (a) S_1 CCA film with rejection wavelength at 428 nm and 525 nm, (b) S_2 film with rejection wavelength at 517 nm and 551 nm, and (c) S_3 film with rejection wavelength at 617 nm and 746 nm.

3.3.1 Radioluminescence spectra

For each set of CCA particles encapsulated in hydrogels, emission spectra were compared before and after shifting the rejection wavelength to overlap the targeted emitter (cf. **Figure 3.6**). In each case, an overall decrease in emission of the targeted emitter was observed with varying levels of suppression. Notably, **Figure 3.6c** shows that only the emission of RMMA in the S_3 film was affected while NMMA emission remained largely unchanged. This suggests that the rejection wavelength causes only a local suppression of the radioluminescence.

The rejection wavelength of the S_1 gel was shifted from 528 nm to 428 nm, and the total observed radioluminescence decreased by 26%. The weakest suppression observed for a targeted emitter was a 10% decrease in the NMMA emission in the S_2 gels with a rejection wavelength shift from 551 nm to 517 nm. For a liquid CCA system with a single crystal, a distinct drop in the emission is expected, as demonstrated by Burdette et al [1]. However, studies have shown that defects present in the crystalline array of particles affect the optical characteristics in multiple ways, such as broadening the bandwidth or lessening the intensity of the bandgap [58, 59]. Furthermore, a previous experiment suggests that embedding the CCA particles in a hydrogel network inherently introduces defects to the system[28]. One source of defects during encapsulation could be non-uniform photopolymerization throughout the film's thickness. The defects incorporated into the CCAs during photopolymerization in situ with the hydrogel network result in multiple crystals within the same film, all with slightly different interplanar spacing. Additionally, there is non-uniform evaporation of water out of the hydrogels because the edges dry out sooner. Combining the inherent defects with the uneven drying results in CCAs with non-uniform photonic bandgaps. Variance in the rejection wavelength causes radioluminescence

suppression to occur at multiple wavelengths, resulting in a general reduction in the emission instead of a sharp decrease.

3.3.2 Difference in emissions

The difference of the two collected emission spectra for each CCA hydrogel is expected to primarily center around the reflectance observed when the rejection wavelength has been shifted to overlap the emission. Although the reflectance was within the region in which a decreased emission occurred for each hydrogel, the difference curves were broader than the reflectance or were not the expected shape. It is supposed that the broadness of the radioluminescence suppression is caused by previously discussed defects in the crystal structure of the CCAs within the films. The shape of the difference curve for the S_1 film (cf. **Figure 3.7a**) appears to have two separate regions of emission suppression at 424 nm 447 nm. However, these peaks mirror two peaks of AMMA emission nearly exactly, and the shape of the difference curve for the S_3 film (cf. **Figure 3.7c**) also mirrors that of the initial emission of RMMA. When the percentage of emission that is blocked is considered for each point (cf. **Figure 3.8**), a singular depression is observed for each of the films. Each observed rejection wavelength is located within these depressions, while the broadness of the depression corresponds with the relative amount of defects within the crystalline structure embedded in the films. Because the emission suppression was shallowest and over the broadest range, the S_2 film is suggested to have the most defects within its structure. The partial bandgap had the highest intensity in the S_1 gel, with a maximum blocked emission of ca. 27%, while the distribution of rejection wavelengths was narrowest in the S_3 film.

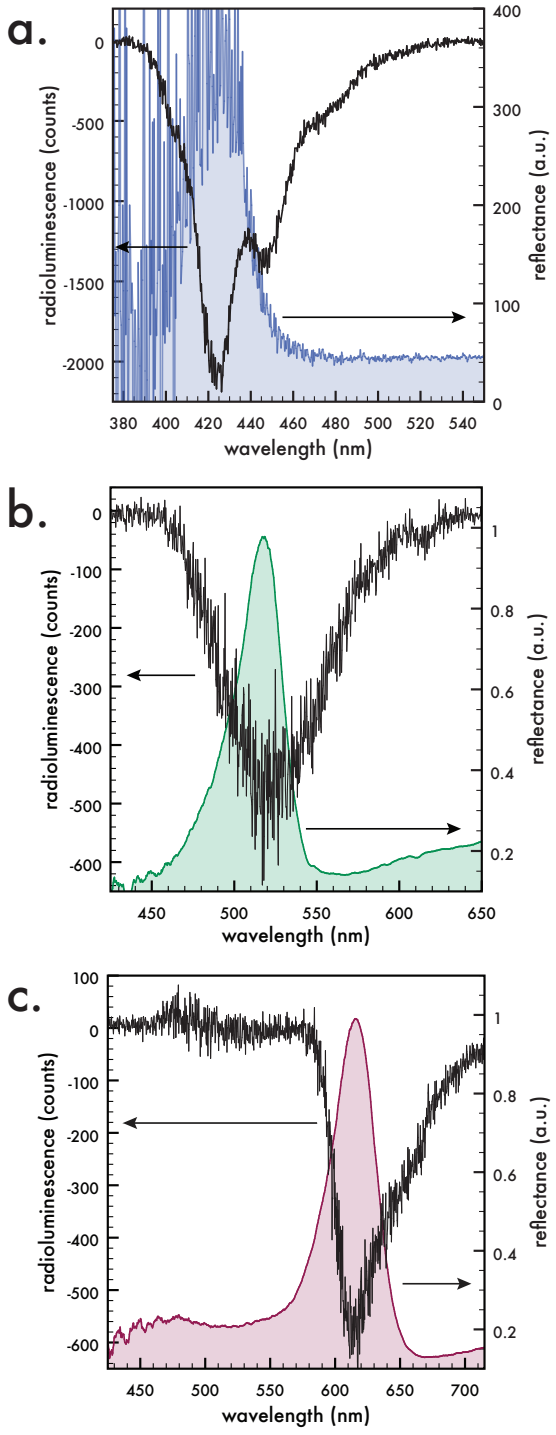

Figure 3.7: Difference between the emission spectra for films of each CCA series compared to the rejection wavelength corresponding to the suppressed emission; reflectance observed from a small area of the CCA film. (a) S_1 CCA film with reflectance (blue) at 428 nm, (b) S_2 film with reflectance (green) at 517 nm, and (c) S_3 film with reflectance (red) at 617 nm.

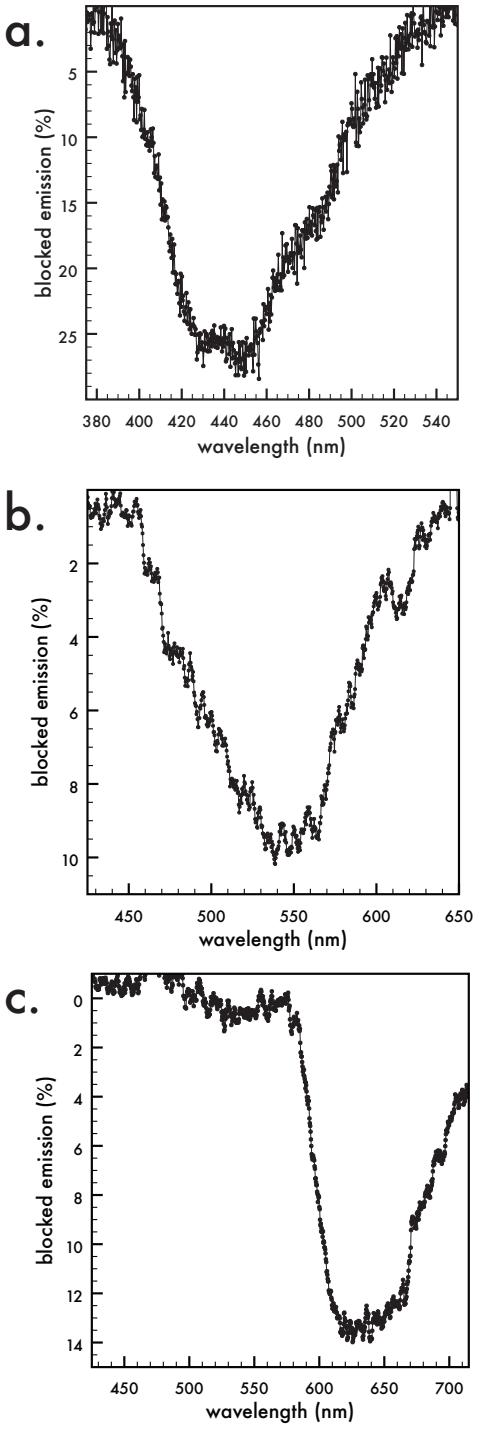

Figure 3.8: The percentage of initial emission blocked at each point based on the two spectra from **Figure 3.6**. (a) S_1 CCA film, (b) S_2 film, and (c) S_3 film.

Chapter 4

Final Remarks

4.1 Conclusion

The effort presented in this work demonstrated the effect of a rejection wavelength on the exhibited radioluminescence of a crystalline colloidal array (CCA) encapsulated in a poly(ethylene glycol) methacrylate (PEGMA) based hydrogel network. The CCA films presented were manipulated to emit across the entire visible light spectrum by covalently incorporating fully organic emitters into the CCAs. The CCAs exploited an organic radioluminescent dye as the basis for emission upon excitation with x-rays; the emissions were shifted across the visible light spectrum through judicious selection of fluorescent dyes to form sequential Förster resonance energy transfer (FRET) pairs. The first FRET paired consisted of the radioluminescent dye, an anthracene derivative, as the donor and a fluorescent dye, a naphthalimide derivative, as the acceptor. The pairing demonstrated an efficient and total energy transfer. The second FRET pair was comprised of the naphthalimide derivative as the donor and another fluorescent dye, a rhodamine B derivative, as the acceptor, and this pairing demonstrated a marginally less efficient energy transfer. Three unique CCA

series were used in this work for overall emissions spanning the visible light spectrum upon irradiation with x-rays: blue light from S_1 CCA hydrogels, green light from S_2, and red light from S_3. The anthracene component absorbs x-rays and subsequently either emits blue light or transfers the energy in the presence of the naphthalimide component, which then either emits green light or transfers energy to the rhodamine B component included. The rejection wavelength resultant from the long-range ordering of the monodisperse poly(styrene-co-propargyl acrylate) based nanoparticles forming the CCAs served as a tool to tailor the radioluminescence by forbidding the propagation of photons at specific wavelengths of light in the visible spectrum, thus suppressing the emission at those wavelengths. The position of the rejection wavelength was controlled via the volume of the CCA hydrogel, which was modified by drying and swelling the hydrogel network. Since the diffracted light is proportional to the interplanar spacing of the CCA, this effectively blue- and red-shifted the rejection wavelength. Defects in the crystalline array affected the range and intensity of radioluminescence suppression. Ultimately, the emission of the CCA films was tuned by coupling the emitters incorporated with the partial bandgap.

4.2 Future Work

It is recommended to find methods to mitigate defect formation while photopolymerizing a hydrogel network in situ with the CCA to develop a CCA hydrogel with a singular, uniform rejection wavelength with a narrow bandwidth. Alternatively, an experimental setup that examines the same area for both reflectance and emission would present a more accurate assessment of the optical properties of the system. A narrower observed reflectance that is consistent across the area for which the emission was collected should lead to a more distinct suppression of the radiolu-

minescence, creating a more specifically tunable emission.

As the CCA hydrogels are inherently quite fragile, a reinforced network could provide the means to observe the hydrogels through repeated cycles of drying and swelling to examine the change in optical characteristics over time. Currently, only one cycle of drying and swelling was able to be observed for the films before cohesive failure occurred, so there is a demonstrated reason for improvement.

Appendices

Appendix A Synthesis of organic emitter compounds

A.1 Anthracene methyl methacrylate derivative (AMMA)

Anthracen-9-ylmethyl methacrylate (AMMA) was synthesized using a modified method described elsewhere[60]. 9-Anthracene methanol (97% Alfa Aesar) (4 g, 19.2 mmol) was dissolved in 30 mL dichloromethane, then trimethylamine was added. The obtained solution was cooled to -5 °C. Methacryloyl chloride was added dropwise to the stirred cooled solution and the obtained mixture was allowed to reach room temperature and was stirred for 6 hours (cf. **Figure 1**). The mixture was washed with water and the organic solution was separated and dried with Na_2SO_4, filtered and evaporated under vacuum. The product was purified by flash column chromatography. Solvent dichloromethane-hexane (1:1), Rf=0.5. Product was recrystallized from hexane. Yield 3.9 g (73%). ^{1}H NMR (300 MHz, $CDCl_3$, δ, ppm): 1.92 (s, 3H), 5.51 (t, 1H), 6.06 (t, 1H), 6.22 (s, 2H), 7.50 (m, 2H, J =7.6 Hz, J =6.9 Hz), 7.58 (m, 2H, J =7.6 Hz, J =6.9 Hz), 8.03 (d, 2H, J =8.9 Hz), 8.38 (d, 2H, J =8.9 Hz), 8.52 (s, 1H).

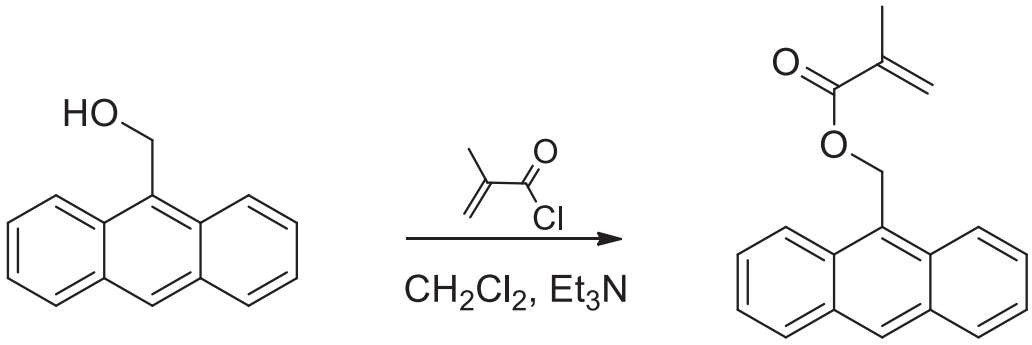

Figure 1: Synthetic scheme to yield anthracen-9-ylmethyl methacrylate (AMMA).

A.2 Naphthalimide methyl methacrylate derivative (NMMA)

2-(2-Hydroxyethyl)-6-(piperidin-1-yl)-1H-benzo-[de]isoquinoline-1,3(2H)-dione (**1**) was synthesized according to a previously described method[61].

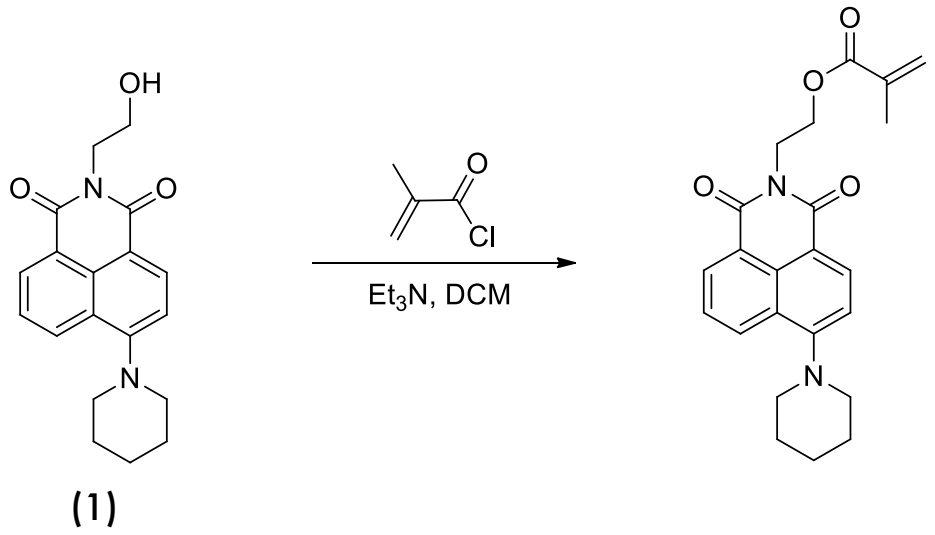

Figure 2: Synthetic scheme to yield 1,3-dioxo-6-(piperidin-1-yl)-1H-benzo[de]isoquinolin-2(3H)-yl)ethyl methacrylate (NMMA).

2-(1,3-Dioxo-6-(piperidin-1-yl)-1H-benzo-[de]isoquinolin-2(3H)-yl)ethyl methacrylate (NMMA) was synthesized by first dissolving (**1**) (0.52 g, 1.6 mmol) and trimethylamine (0.21 g, 2.1 mmol) in dry dichloromethane. The solution was cooled to -5°C. Methacryloyl chloride (0.2 g, 1.92 mmol) was added dropwise to the stirred solution. The obtained mixture was stirred at -5 °C for 30 minutes, then the cooling bath was removed and the reaction was stirred at room temperature for an additional 3 hours (cf. **Figure 2**). The mixture was washed with water, and the organic layer was separated, dried with Na_2SO_4, filtered, and evaporated under vacuum at 30°C. The residue was recrystallized from methanol/hexane (5/1) mixture, filtered, washed with hexane and dried. Yield 0.37 g (59%), yellow solid, m.p=136 °C. ^{1} NMR ($CDCl_3$) δ 1.74 (m, 2H), 1.86 (s, 3H), 1.89 (m, 4H, J=5.2 Hz), 3.23 (t, 2H, J=5.2 Hz), 4.48 (d,

2H, J=4.8 Hz), 4.53 (d, 2H, J=4.8 Hz), 5.5 (s, 1H), 6.05 (s, 1H), 7.17 (d, 1H, J=7.9 Hz), 7.68 (d.d, 2H, J=8.3 Hz, J=7.2 Hz, J=1.0 Hz), 8.39 (d.d, 1H, J=8.3 Hz, J=1.0 Hz), 8.49 (d, 1H, J=7.9 Hz), 8.57 (d.d, 1H, J=7.2 Hz, J=1.0 Hz).

A.3 Rhodamine B methyl methacrylate derivative (RMMA)

N-(6-(Diethylamino)-9-(2-((2-(methacryloyloxy)-ethoxy)carbonyl)phenyl)-3H-xanthen-3-ylidene)-N-ethylethanaminium chloride (RMMA) was synthesized using a modified method described elsewhere[62]. Rhodamine B acid chloride (0.42 g, 0.84 mmol) and 2-hydroxyethyl methacrylate (0.14 g, 1.09 mmol) were dissolved in dry dichloromethane (8 mL). The obtained solution was cooled to 0°C and degassed with nitrogen. Next, trimethylamine (0.13 g, 1.28 mmol) was added into the stirred solution (cf. **Figure 3**). The cooling was removed and the mixture was stirred at room temperature for 6 hours, washed with water, dried with Na_2SO_4, filtered, and evaporated under reduced pressure at 35 °C. Crude residue was purified by column chromatography on silica. First solvent dichloromethane/methanol (20/1) to wash out impurities, second solvent dichloromethane/methanol (10/1) to wash out a product, Rf = 0.25. Yield 0.33 g (71%), dark-red oil. ^{1}H NMR ($CDCl_3$) δ 1.32 (t, 12H, J=7.2 Hz), 1.88 (t, 3H, J=1.3 Hz), 3.64 (q, 8H, J=7.2 Hz), 4.18 (m, 2H, J=2.4 Hz), 4.30 (m, 2H, J=2.4 Hz), 5.55 (t, 1H, J=1.7 Hz), 6.02 (t, 1H, J=1.4 Hz), 6.79 (d, 2H, J=2.4 Hz), 6.91 (d.d, 2H, J=2.4 Hz, J=9.3 Hz), 7.05 (d, 2H, J=9.3 Hz), 7.32 (d.d, 1H, J=1.0 Hz, J=7.6 Hz), 7.74 (m, 1H, J=1.4 Hz, J=7.6 Hz), 7.83 (m, 1H, J=1.4 Hz J=7.6 Hz) 8.29 (d, 1H, J=1.0 Hz, J=7.6 Hz).

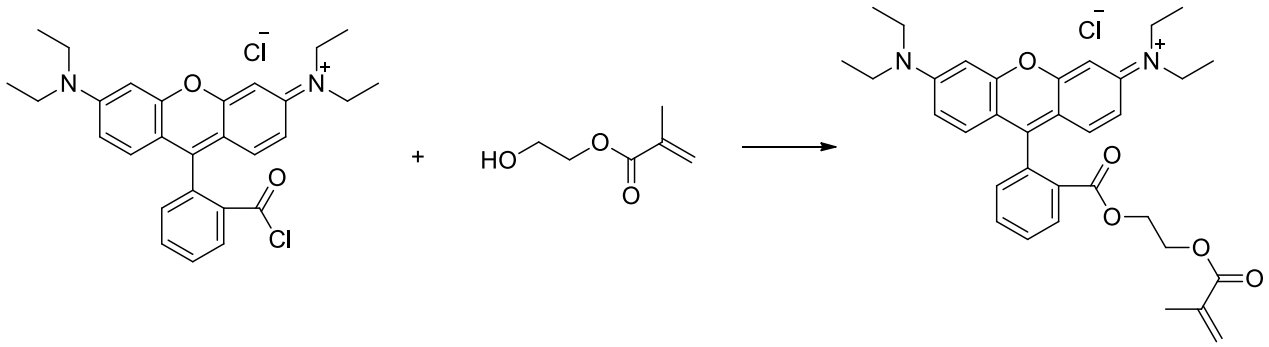

Figure 3: Synthetic scheme to yield N-(6-(diethylamino)-9-(2-((2-(methacryloyloxy)ethoxy)carbonyl)phenyl)-3H-xanthen-3-ylidene)-N-ethylethanaminium chloride (RMMA).

Bibliography

[1] Mary K. Burdette, Yuriy P. Bandera, Gary M. Gray, and Stephen H. Foulger. Dynamic emission tuning of x-ray radioluminescent crystalline colloidal arrays: Coupling the optical stop band with sequential forster resonance energy transfers. *Advanced Optical Materials*, 7(2), 2019.

[2] T. Paik, T. R. Gordon, A. M. Prantner, H. Yun, and C. B. Murray. Designing tripodal and triangular gadolinium oxide nanoplates and self-assembled nanofibrils as potential multimodal bioimaging probes. *ACS Nano*, 7(3):2850–2859, 2013.

[3] C. M. Carpenter, C. Sun, G. Pratx, R. Rao, and L. Xing. Hybrid x-ray/optical luminescence imaging: Characterization of experimental conditions. *Medical Physics*, 37(8):4011–4018, 2010.

[4] T. Guo, Y. Lin, W. J. Zhang, J. S. Hong, R. H. Lin, X. P. Wu, J. Li, C. H. Lu, and H. H. Yang. High-efficiency x-ray luminescence in Eu3+-activated tungstate nanoprobes for optical imaging through energy transfer sensitization. *Nanoscale*, 10(4):1607–1612, 2018.

[5] L. Sudheendra, G. K. Das, C. Q. Li, D. Stark, J. Cena, S. Cherry, and I. M. Kennedy. NaGdF4:Eu3+ nanoparticles for enhanced x-ray excited optical imaging. *Chemistry of Materials*, 26(5):1881–1888, 2014.

[6] X. L. Li, Z. L. Xue, M. Y. Jiang, Y. B. Li, S. J. Zeng, and H. R. Liu. Soft x-ray activated NaYF4:Gd/Tb scintillating nanorods for in vivo dual-modal x-ray/x-ray-induced optical bioimaging. *Nanoscale*, 10(1):342–350, 2018.

[7] N. Lee, S. H. Choi, and T. Hyeon. Nano-Sized CT Contrast Agents. *Advanced Materials*, 25(19):2641–2660, 2013.

[8] A. Reisch and A. S. Klymchenko. Fluorescent polymer nanoparticles based on dyes: Seeking brighter tools for bioimaging. *Small*, 12(15):1968–1992, 2016.

[9] C. Zheng, M. Zheng, P. Gong, D. Jia, P. Zhang, B. Shi, Z. Sheng, Y. Ma, and L. Cai. Indocyanine green-loaded biodegradable tumor targeting nanoprobes for in vitro and in vivo imaging. *Biomaterials*, 33(22):5603–5609, 2012.

[10] M. Peuster, C. Fink, and C. von Schnakenburg. Biocompatibility of corroding tungsten coils: in vitro assessment of degradation kinetics and cytotoxicity on human cells. *Biomaterials*, 24(22):4057–4061, 2003.

[11] T. J. Haley, A. M. Flesher, N. Komesu, H. C. Upham, J. Cawthorne, and L. Mavis. Pharmacology and toxicology of terbium, thulium, and ytterbium chlorides. *Toxicology and Applied Pharmacology*, 5(4):427–436, 1963.

[12] G. Q. Zhou, Y. F. Li, Y. Y. Ma, Z. Liu, L. L. Cao, D. Wang, S. D. Liu, W. S. Xu, and W. Y. Wang. Size-dependent cytotoxicity of yttrium oxide nanoparticles on primary osteoblasts in vitro. *Journal of Nanoparticle Research*, 18(5), 2016.

[13] G. F. Knoll. *Radiation detection and measurement*. John Wiley and Sons, 2010.

[14] J. B. Birks. *The Theory and Practice of Scintillation Counting*. Pergamon Press Ltd., 1 edition, 1964.

[15] J.S. Klein, C. Sun, and G. Pratx. Radioluminescence in biomedicine: Physics, applications, and models. *Phys. Med. Biol.*, 64(4), 2019.

[16] J. B. Birks. Scintillations from organic crystals - specific fluorescence and relative response to different radiations. *Proceedings of the Physical Society of London Section A*, 64(382):874–877, 1951.

[17] G. T. Wright. Absolute scintillation efficiency of anthracene crystals. *Proceedings of the Physical Society of London Section B*, 68:929–937, 1955.

[18] S. Beddar and L. Beaulieu. *Scintillation Dosimetry*. CRC Press, Boca Raton, FL, 1 edition, 2016.

[19] Jerome W. Sidman. Electronic and vibrational states of anthracene. *The Journal of Chemical Physics*, 25(1):115–121, 1956.

[20] P. Andrew and W. L. Barnes. Forster energy transfer in an optical microcavity. *Science*, 290(5492):785–788, 2000.

[21] H. T. Dung, L. Knoll, and D. G. Welsch. Intermolecular energy transfer in the presence of dispersing and absorbing media. *Physical Review A*, 65(4), 2002.

[22] D. L. Andrews. A unified theory of radiative and radiationless molecular energy transfer. *Chem. Phys.*, 135(2):195–201, 1989.

[23] D. L. Andrews and J. Rodriguez. Resonance energy transfer: spectral overlap, efficiency, and direction. *J Chem Phys*, 127(8):084509, 2007.

[24] Y. S. Papir, M. E. Woods, and I. M. Krieger. Monodisperse latices iii: Cross-linked polystyrene latices. *J. Paint Technol.*, 42(550):571–578, 1970.

[25] J. M. Jethmalani and W. T. Ford. Diffraction of visible light by ordered monodisperse silica-poly(methyl acrylate) composite films. *Chemistry of Materials*, 8(8):2138–2146, 1996.

[26] P.A. Rundquist, P. Photinos, S. Jagannathan, and S.A. Asher. Dynamical bragg diffraction from crystalline colloidal arrays. *J. Chem. Phys.*, 91(8):4932–4941, 1989.

[27] S.A. Asher, J. Holtz, L. Liu, and Z. Wu. Self-assembly motif for creating submicron periodic materials. polymerized crystalline colloidal arrays. *J. Am. Chem. Soc.*, 116:4997–4998, 1994.

[28] S. H. Foulger, P. Jiang, Y. Ying, A. Lattam, D. Smith Jr, and J. Ballato. Photonic bandgap composites. *Advanced Materials*, 13(24):1898–1901, 2001.

[29] D. Evanoff Jr, S. Hayes, Y. Ying, G. H. Shim, J. R. Lawrence, J. B. Carroll, R. D. Roeder, J. M. Houchins, C. F. Huebner, and S. H. Foulger. Functionalization of crystalline colloidal arrays through click chemistry. *Advanced Materials*, 19(21):3507–3512, 2007.

[30] P. A. Hiltner and I. M. Krieger. Diffraction of light by ordered suspensions. *J. Phys. Chem.*, 73:2386, 1969.

[31] N. Clark, A. Hurd, and B. Ackerson. Single colloidal crystals. *Nature*, 281(5726):57–60, 1979.

[32] Y. Monovoukas and A. P. Gast. Microstructure identification during crystallization of charged colloidal suspensions. *Phase Transitions*, 21:183, 1990.

[33] Y. Monovoukas and A. P. Gast. The experimental phase diagram of charged colloidal suspensions. *J. Colloid Interface Sci.*, 128(2):533–548, 1989.

[34] W. L. Vos, R. Sprik, A. vanBlaaderen, A. Imhof, A. Lagendijk, and G. H. Wegdam. Strong effects of photonic band structures on the diffraction of colloidal crystals. *Physical Review B*, 53(24):16231–16235, 1996.

[35] V. N. Bogomolov, S. V. Gaponenko, I. N. Germanenko, A. M. Kapitonov, E. P. Petrov, N. V. Gaponenko, A. V. Prokofiev, A. N. Ponyavina, N. I. Silvanovich, and S. M. Samoilovich. Photonic band gap phenomenon and optical properties of artificial opals. *Physical Review E*, 55(6):7619–7625, 1997.

[36] Y. N. Xia, B. Gates, and S. H. Park. Fabrication of three-dimensional photonic crystals for use in the spectral region from ultraviolet to near-infrared. *Journal of Lightwave Technology*, 17(11):1956–1962, 1999.

[37] S. H. Foulger, P. Jiang, A. C. Lattam, D. W. Smith, and J. Ballato. Mechanochromic response of poly(ethylene glycol) methacrylate hydrogel encapsulated crystalline colloidal arrays. *Langmuir*, 17(19):6023–6026, 2001.

[38] J. H. Holtz and S.A. Asher. Polymerized colloidal crystal hydrogel films as intelligent chemical sensing materials. *Nature*, 389:829–832, 1997.

[39] M. K. Burdette, H. W. Jones, Y. Bandera, and S. H. Foulger. X-ray radioluminescent hydrogel stabilized crystalline colloidal arrays. *Opt. Mater. Express*, 9(3):1416–1429, 2019.

[40] S. Zalipsky and J. M. Harris. *Poly(ethylene glycol): Chemistry and Biological Applications*, volume 680. American Chemical Society, 1997.

[41] A. K. Yetisen, H. Butt, L. R. Volpatti, I. Pavlichenko, M. Humar, S. J. J. Kwok, H. Koo, K. S. Kim, I. Naydenova, A. Khademhosseini, S. K. Hahn, and S. H. Yun. Photonic hydrogel sensors. *Biotechnology Advances*, 34(3):250–271, 2016.

[42] Vladimir L. Alexeev, Anjal C. Sharma, Alexander V. Goponenko, Sasmita Das, Igor K. Lednev, Craig S. Wilcox, David N. Finegold, and Sanford A. Asher. High ionic strength glucose-sensing photonic crystal. *Anal. Chem.*, 75:2316–2323, 2003.

[43] Matti Ben-Moshe, Vladimir L. Alexeev, and Sanford A. Asher. Fast responsive crystalline colloidal array photonic crystal glucose sensors. *Anal. Chem.*, 78(14):5149–5157, 2006.

[44] Sanford A. Asher, Serban F. Peteu, Chad E. Reese, Ming Xiang Lin, and David Finegold. Polymerized crystalline colloidal array chemical sensing materials for detection of lead in bodily fluids. *Anal. Bioanal. Chem.*, 373:632–638, 2002.

[45] Chad E. Reese and Sanford A. Asher. Photonic crytal optrode sensor for detection of pb2+ in high ionic strength environments. *Anal. Chem.*, 75(15):3915–3918, 2003.

[46] Anjal C. Sharma, Tushar Jana, Rasu Kesavamoorthy, Lianjun Shi, Mohamed A. Virji, David N. Finegold, and Sanford A. Asher. A general photonic crystal sensing motif: Creatinine in bodily fluids. *J. Am. Chem. Soc.*, 126:2971–2977, 2004.

[47] Fei Xue, Zihui Meng, Fenglian Qi, Min Xue, Fengyan Wang, Wei Chen, and Zequn Yan. Two-dimensional inverse opal hydrogel for ph sensing. *Analyst*, 139:6192–6196, 2014.

[48] Xiangling Xu, Alexander V. Goponenko, and Sanford A. Asher. Polymerized polyhema photonic crystals: ph and ethanol sensor materials. *J. Am. Chem. Soc.*, 130(10):3113–3119, 2008.

[49] Toshimitsu Kanai, Hiroki Yano, Naoto Kobayashi, and Tsutomu Sawada. Enhancement of thermosensitivity of gel-immobilized tunable colloidal photonic crystals with anisotropic contraction. *ACS Macro Lett.*, 6:1196–1200, 2017.

[50] Youfeng Yue, Takayuki Kurokawa, Md Anamul Haque, Tasuku Nakajima, Takayuki Nonoyama, Xufeng Li, Itsuro Kajiwara, and Jian Ping Gong. Mechano-actuated ultrafast full-colour switching in layered photonic hydrogels. *Nat Commun*, 5, 2014.

[51] Y. Kuang, G. Pratx, M. Bazalova, B. W. Meng, J. G. Qian, and L. Xing. First demonstration of multiplexed x-ray fluorescence computed tomography (xfct) imaging. *IEEE Transactions on Medical Imaging*, 32(2):262–267, 2013.

[52] Ehsan Eftekhari, Ivan S. Cole, and Qin Li. The effect of fluorophore incorporation on fluorescence enhancement in colloidal photonic crystals. *Physical Chemistry Chemical Physics*, 18(3):1743–1749, 2016.

[53] Edwin A. Chandross, J. Ferguson, and E. G. McRae. Absorption and emission spectra of anthracene dimers. *The Journal of Chemical Physics*, 45(10):3546–3553, 1966.

[54] J. Ren, X. L. Zhao, Q. C. Wang, C. F. Ku, D. H. Qu, C. P. Chang, and H. Tian. Synthesis and fluorescence properties of novel co-facial folded naphthalimide dimers. *Dyes and Pigments*, 64(2):179–186, 2005.

[55] C. Blum, N. Zijlstra, A. Lagendijk, M. Wubs, A. P. Mosk, V. Subramaniam, and W. L. Vos. Nanophotonic control of the forster resonance energy transfer efficiency. *Physical Review Letters*, 109(20), 2012.

[56] Sunita Kedia and Sucharita Sinha. Energy transfer from rhodamine-b to oxazine-170 in the presence of photonic stop band. *Optics Communications*, 339:41–46, 2015.

[57] W. B. Wu, M. L. Wang, Y. M. Sun, W. Huang, Y. P. Cui, and C. X. Xu. Fluorescent polystyrene microspheres with large stokes shift by fluorescence resonance energy transfer. *Journal of Physics and Chemistry of Solids*, 69(1):76–82, 2008.

[58] Y. A. Vlasov, V. N. Astratov, A. V. Baryshev, A. A. Kaplyanskii, O. Z. Karimov, and M. F. Limonov. Manifestation of intrinsic defects in optical properties of self-organized opal photonic crystals. *Phys. Rev. E*, 61(5):5784–5793, 2000.

[59] Y. Ye, F. LeBlanc, A. Haché, and V. Truong. Self-assembling three-dimensional colloidal photonic crystal structure with high crystalline quality. *Applied Physics Letters*, 78(1):52–54, 2001.

[60] C. Bilir, T. Erdogan, S. Odabas, and E. Unveren. Novel partially fluorinated graft block copolymer ionomer as potential proton exchange membrane material. *Polymer*, 95:91–101, 2016.

[61] N. R. Chereddy, S. Thennarasu, and A. B. Mandal. A highly selective and efficient single molecular fret based sensor for ratiometric detection of fe3+ ions. *Analyst*, 138(5):1334–7, 2013.

[62] J. Morales-Sanfrutos, J. Lopez-Jaramillo, M. Ortega-Munoz, A. Megia-Fernandez, F. Perez-Balderas, F. Hernandez-Mateo, and F. Santoyo-Gonzalez. Vinyl sulfone: A versatile function for simple bioconjugation and immobilization. *Org Biomol Chem*, 8(3):667–75, 2010.